

Original Research

Effects of Dissolved Organic Matter with Different Molecular Weights on Antimony Mobilization in Shallow Groundwater at the World's Largest Antimony Mine, China

Chunming Hao^{1,2,3}, Feilin Deng³, Kaikai He³, Qiong Li^{3*}

¹Key Laboratory of Natural Resource Coupling Process and Effects, Beijing, 100055, China

²Key Laboratory of Mine Geological Hazards Mechanism and Control, Ministry of Natural Resources, Xi'an, Shaanxi, 710054, P.R. China

³North China Institute of Science and Technology, Sanhe, Hebei, 065201, P.R. China

Received: 29 April 2024

Accepted: 12 June 2024

Abstract

The molecular weight is a fundamental property of dissolved organic matter (DOM) that affects the fate of arsenic (As) in groundwater. However, there is limited knowledge regarding the various molecular weights on the geochemical transformation mechanisms of DOM with respect to antimony (Sb) migration in groundwater. A total of 20 samples were collected from high- and low-Sb D_3X^4 waters in the world's largest antimony mine to evaluate the effects of different molecular weights of DOM on Sb mobilization using a sequential ultrafiltration technique. Dissolved Sb occurred mainly in the <1kDa fraction, while total Fe (TFe) colloids and DOM mostly existed in <0.45- μ m and <100-kDa fractions, respectively. A protein-like component with a higher biological index (BIX), lower humification index (HIX), and specific ultraviolet absorbance ($SUVA_{254}$) demonstrated a higher binding potential to Sb. Owing to the lower values of $\delta^{13}C_{DIC}$ and the difference between $\delta^{13}C_{DIC}$ and $\delta^{13}C_{DOC}$, the microbial degradation of DOM had a substantial contribution to Sb mobility in the D_3X^4 water. The results obtained from this research contribute to our comprehension of the biogeochemical behavior of antimony in shallow groundwater.

Keywords: molecular weight, excitation-emission matrix spectroscopy, parallel factor analysis, stable carbon isotopes, dissolved organic matter, antimony

*e-mail: hdliqiong@163.com

Tel.: +86-1061591480

Introduction

Antimony (Sb), an element with metalloid properties that is toxic and carcinogenic, is commonly acknowledged as a major environmental contaminant according to both the United States and the European Union [1-5]. Excessive levels of Sb in groundwater ($>5.00 \mu\text{g/L}$) are a global environmental concern across different regions worldwide, such as China [5, 6], Australia [7], Scotland [8], France [9], Canada [10, 11], Italy [12], and Egypt [13]. The primary natural routes for the infiltration of antimony (b) into groundwater were through oxidation and dissolution of Sb-bearing sulfides, such as stibnite (Sb_2S_3) and Jamesonite ($\text{Pb}_4\text{FeSb}_6\text{S}_{14}$) [1, 11, 14-16]. Moreover, human activities such as mining and the burning of fossil fuels and waste materials have considerably enhanced the mobility and distribution potential of Sb in groundwater systems [16-19].

Dissolved organic matter (DOM) encompasses humic acids, fulvic acids, and proteins, which play a crucial role in the biogeochemical mobilization of Sb within groundwater [17, 20-24]. The presence of DOM could increase higher adsorption affinity for Fe hydroxide surfaces and facilitate the release of Sb [17, 25], while also forming complexes with Sb to improve its solubility [20, 21, 26, 27]. In addition, in the presence of sunlight, DOM have the potential to enhance the conversion of Sb(III) to Sb(V), thereby accelerating the movement of Sb in naturally occurring oxygenated environments [22, 23, 28]. The utilization of bio-reactive DOM had been found to enhance the autotrophic capabilities of microorganisms, thereby facilitating the oxidative dissolution of minerals containing Sb, such as stibnite [29, 30].

The molecular weight is widely recognized as a fundamental characteristic of DOM and plays a crucial role in influencing the interaction between DOM and metals [31-33]. In general, metals tend to exhibit a preference for DOM with varying molecular weights due to their distinct binding affinities [31, 33]. In natural aquatic environments, the mobilization of As is facilitated by its strong affinity for medium-molecular-weight DOM (MDOM) (1-10 kDa) and low-molecular-weight DOM (LDOM) (below 1 kDa) [32-35]. In addition to impacting the affinity for metal binding, amino acids containing LDOM exhibited bioactivity and were readily metabolized by microorganisms [36, 37].

Hence, comprehending the functional and molecular properties of DOM is crucial in investigating its involvement in the mobilization of As within natural aquatic environments. Despite the fact that As and Sb possess identical configurations of outer-orbital electrons (s^2p^3), it has been commonly assumed that their geochemical behaviors, which are influenced by DOM, tend to be similar [1, 17, 38]. Moreover, molecular weight fractions of DOM have been confirmed to affect the As mobilization in groundwater [17]. However, the impact of various molecular weight fractions of DOM on Sb pollution in groundwater remains poorly

understood, thereby enhancing our comprehension of differences in Sb and As enrichment mechanisms within groundwater systems. Therefore, it is crucial to gain a comprehensive understanding of the source, characteristics, and geochemical reactivity of DOM with distinct molecular properties to elucidate the enrichment of Sb in groundwater.

The use of fluorescence spectroscopy has yielded significant knowledge regarding the nature, origin, and composition of DOM in groundwater [39-41]. Furthermore, the utilization of EEM-PARAFAC, a technique that combines excitation-emission matrix fluorescence with parallel factor analysis, has been extensively applied in identifying the origins and constituents of DOM owing to its quickness, cost-effectiveness, and accuracy [37, 42-45]. Recently, successful applications of molecular weight separation techniques have been observed in the assessment of metal distributions in DOM with different molecular weights in groundwater [32, 33, 46]. Changes in fluorescence offered valuable insights into identifying the unique fluorescence properties linked to different molecular weights of DOM [23, 33, 34].

Hence, the distribution and movement of Sb in shallow groundwater were investigated by analyzing the optical properties of DOM with varying molecular weights. This study aimed to (1) examine the spectroscopic characteristics and chemical properties of DOM with different molecular weights at various Sb concentrations and (2) assess the influence of DOM with different molecular weights on Sb mobilization in shallow groundwater. The findings from this study enhance our understanding of the mechanisms behind Sb enrichment in shallow groundwater.

Materials and Methods

Study Area

As the world's largest antimony mine, the Xikuangshan mine is situated in central China, specifically 13 km north of Lengshuijiang City. It spans across a vast area of 26 km^2 and is located within mountainous terrain that runs from northeast to southwest, with elevations ranging between 220 and 823.2 m. The climate is known for its high humidity, with an average annual precipitation of 1381.60 mm, evaporation reaching 903.30 mm, and temperatures averaging 16.7°C from 1949 to 2012. The primary watercourses in the mining region that flow into the Zijiang River include the Xuanshan River, Qingfeng River, Feishuiyan Stream, Tanjia Stream, and Batangshan Stream. The Xikuangshan mine is internationally recognized as "The World's Antimony Capital", earning an impressive reserve of around 2.50 million tons of Sb [1, 17, 47, 48].

The Xikuangshan Sb mine area is situated in a hydrogeologically isolated region, enclosed by

the NE30°-oriented fault NO.75 from the east and west. It encompasses a lamprophyre vein spanning approximately 10 km. As shown in Fig. 1, the primary aquifers in the mining region consist of the lower Shetianqiao karst aquifer (referred to as D_3s^2 water) and the upper Magunao karst aquifer (known as D_3x^4 water), which have been extensively studied by Wen et al. [5] (2016) and Hao et al. [1, 6]. The Sb ore bodies are located at the top of the silicified limestone layers of the D_3s^2 water, which have no hydraulic connection with D_3x^4 water. The D_3x^4 water, which consists of limestone and sandy limestone with an average thickness measuring 258 m and a hydraulic conductivity of 0.0092 m/d as reported by Wen et al.'s study conducted in 2016 and updated in 2022, plays a crucial role as a primary drinking water source for local residents. The main recharge source for the D_3x^4 water is infiltrated precipitation and agricultural irrigation, while groundwater flows from southeast to northwest in the North Mine and from northeast to southwest in the South Mine, respectively. D_3x^4 water discharge occurs through springs that crop out substantially

and drainages associated with mining activities [4]. The primary hydrochemical facies in unpolluted D_3x^4 water is $Ca-HCO_3-SO_4$ type, and Sb concentration is less than 15 mg/L [4]. Some dwellings, industrial facilities, waste rock, and slag are situated over the D_3x^4 water [6, 49]. Moreover, mining regions extensively cultivate rice, corn, and vegetables as their main agricultural produce [17, 49].

Sample Collection

Based on the previous studies conducted on hydrogeology and geochemistry, a total of 20 springs were selected for sampling D_3x^4 water in February 2023 (Fig. 1a). Prior to collection, the brown plastic sampling bottles underwent sequential rinsing with distilled water and D_3x^4 water samples. All water samples were collected in the field and ultrafiltered sequentially through MilliPore filters (high-density polyethylene (HDPE)) with sequential pore sizes of 0.45- μ m, 100-kDa, and 1-kDa by a cross-flow ultrafiltration system (CFUS, Sartorius Vivaflow®.200) [50].

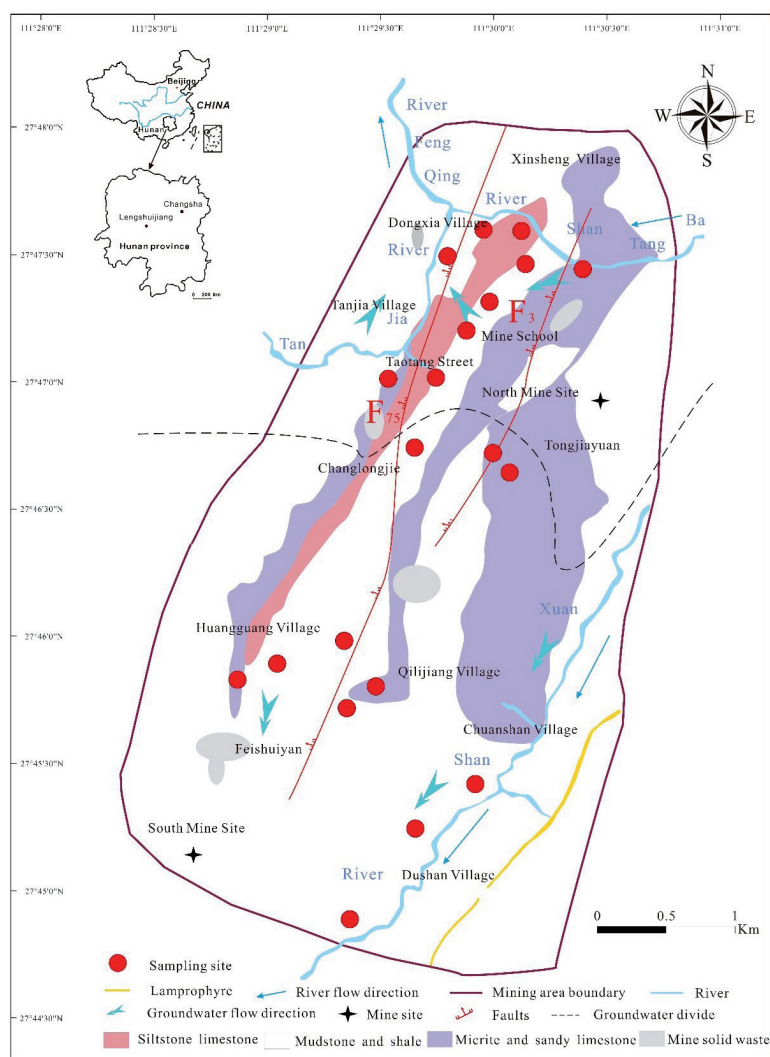


Fig. 1. Location of the study area and distribution of the D_3x^4 water sampling sites from the Xikuangshan mine.

Each of the filtered samples was separated into three categories: high-molecular-weight DOM (HDOM) D_3x^4 water (fraction < 0.45 μm), middle-molecular-weight DOM (MDOM) D_3x^4 water (fraction < 100 kDa), and low-molecular-weight DOM (LDOM) (fraction < 1 kDa). A total of 60 D_3x^4 water samples were obtained during the process of ultrafiltration. The experiment involved utilizing a polymer-enhanced ultrafiltration system with a capacity of 300 mL by pressurizing and filtering with N_2 gas. The ultrafiltration process was previously documented by Dundar et al. [51] and Li et al. [33]. To facilitate the analysis, the collected samples for the major cation and Sb analyses were treated with ultrapure HNO_3 at a ratio of 1:1 (v/v) until reached a pH < 2.0, after which they were promptly stored at a temperature of 4°C in darkness. To prepare samples for stable organic carbon isotope analysis ($\delta^{13}\text{C}_{\text{DOC}}$), they were acidified using 85% H_3PO_4 until the pH was less than 2. For stable inorganic carbon isotope analysis ($\delta^{13}\text{C}_{\text{DIC}}$) was sterilized with HgCl_2 and then collected in HDPE brown glass bottles with 100 mL.

Sample Analysis

The pH and total dissolved solids (TDS) were measured on-site at a sampling location using a portable pH meter (HANNA HI8424, Italy) and a portable conductivity meter (HANNA HI833, Italy), respectively. The concentrations of bicarbonate ions (HCO_3^-) were determined by acid-base titration during field measurements with an analytical precision of 1.0 mg/L. Sb concentrations were determined using a hydride generation atomic fluorescence spectrometer (Qingdao) with a relative standard deviation of $\pm 5\%$ and an analytical precision of 0.10 $\mu\text{g/L}$ [17, 28]. Total Fe (TFe) levels were determined using spectrophotometry (DR2800, HACH, USA) and the phenanthroline method with an analytical precision of 0.01 $\mu\text{g/L}$ [17, 28, 52]. $\delta^{13}\text{C}_{\text{DOC}}$ and $\delta^{13}\text{C}_{\text{DIC}}$ in all samples were determined using isotope ratio mass spectrometry (Trace GC Ultra, Thermo Fisher Scientific, USA) coupled with an online high-precision gas headspace sampler, GasBench (Thermo Fisher Scientific), following the methods of Yu et al. [53] and Zhou et al. [54] with precisions < 0.2‰.

The level of DOM was assessed utilizing a TOC-5000 total organic carbon analyzer from Japan and represented as dissolved organic carbon (DOC), with an analytical accuracy of 0.01 mg/L. The UV-visible spectrophotometer (Hach DR-5000, USA) and the three-dimensional fluorescence spectrophotometer (F7000, Japan) were utilized to perform measurements of ultraviolet-visible and fluorescence in a 10-mm quartz cuvette. Both devices were equipped with a 150-W xenon lamp that does not emit ozone and operated at a consistent temperature of 20°C. The emission wavelength (EM) was scanned from 220 to 550 nm while the excitation wavelength (EX) ranged from 200 to 400 nm, with sampling intervals of 5 nm

during the excitation emission matrices (EEMs) analysis. The fluorescence measurements were conducted with an excitation wavelength step size of 5 nm and an emission wavelength step size of 2 nm. The scan rate was set at 2400 nm/min, the slit width was adjusted to 5 nm, and the amplification voltage used was 700 V.

The spectral overlap was determined by employing PARAFAC modeling with the assistance of fluorescence components from the DOMFluor database [55, 56]. All mean fluorescence intensities are calculated based on three repeated analyses, with subsequent subtraction of blank values and final normalization to Raman units (R.U.). The split half analysis and residual analysis were used to verify the reliability of the three-component model [33]. Residual intensities, were obtained by subtracting the PARAFAC-modeled EEM from the measured EEM maximum deviation of 10% compared to the measured EEM intensities across all samples.

To distinguish DOM sources, the fluorescence index (FI) was determined by dividing the measurement at an emission wavelength of 450 nm by that at 500 nm, after being excited at 370 nm, providing a metric for distinguishing DOM derived from terrestrial and microbial sources [32, 43, 57]. Furthermore, the biological index (BIX), which serves as a measure of indigenous biological activity in aquatics, was determined by dividing the emission intensities at wavelengths of 380 nm and 430 nm under a consistent excitation at 310 nm [58, 59]. In addition, the ratio of the emission scan at 435–480 nm to the emission scan at 300–345 nm with an excitation at 254 nm was utilized for evaluating the humification index (HIX), which serves as an indicator of DOM humification [60–62]. The calculation of the specific ultraviolet absorbance (SUVA_{254}), which is linked to the aromatic nature of organic substances, involved normalizing the UV absorbance at 254 nm with respect to the DOC concentration [36, 59].

To enhance further characterization, the DOM was segregated into two categories. Initially, protein:humic ratios were computed by determining the proportion of protein-like DOM constituents in relation to the total sum of humic-like DOM components. Secondly, the microbial:terrestrial ratios were determined by calculating the proportion of DOM components derived from microorganisms compared to that of terrestrially derived DOM components.

Statistical Analysis

The statistical analysis software, Origin 2021, was employed to establish correlations among all findings. The PARAFAC analysis was performed using the DOM Fluor v.1.7 toolbox in MATLAB (Natick, MA, USA). Descriptive data can be found in Table 1, while Table 2 provides information on the spectroscopic characteristics of DOM components.

Table 1. Geochemistry data for the D₃x₄ water of the Xikuangshan mine area.

Type	Sb	TFe	pH	TDS	HCO ₃ ⁻	DOC	δ ¹³ C _{DOC}	δ ¹³ C _{DIC}
	µg/L			mg/L			‰	
HDOM samples (n = 20)								
Max	20600.00	560.00	8.74	1515	304	10.88	-21.90	-2.30
Min	1.00	0.00	7.14	121	9	2.24	-26.97	-17.04
Mean	3640.74	83.53	8.03	494	173	5.75	-24.41	-9.46
SD	5200.22	135.95	0.34	351	85	2.35	1.51	3.81
MDOM samples (n = 20)								
Max	20800.00	230.00	/	/	149	9.63	-19.00	-2.30
Min	1.00	0.00	/	/	1	1.26	-26.26	-17.84
Mean	3646.61	26.59	/	/	37	3.51	-21.99	-9.21
SD	5225.14	68.35	/	/	115	2.17	2.06	4.24
LDOM samples (n = 20)								
Max	20800.00	30.00	/	/	226	7.74	-16.78	-3.08
Min	1.00	0.00	/	/	1	1.09	-24.70	-16.36
Mean	3619.64	2.59	/	/	71	2.98	-20.76	-9.36
SD	5249.69	7.84	/	/	125	1.64	2.21	2.66

Note: Values below the LOD are set to zero for statistical purposes.

Results

General Hydrochemistry Characterization of D₃x₄ Waters with Different Molecular Weights

According to the geogenic values without pollution [5, 6], the D₃x₄ water samples were categorized into two groups: low-Sb groundwater (<15.00 µg/L) and high-Sb groundwater (>15.00 µg/L). pH values ranging from 7.14 to 9.74 with a mean of 8.03 were observed (Table 1), indicating a weakly alkaline environment in all D₃x₄ waters. The phenomenon indicated that H⁺ produced from stibnite oxidation had been immediately neutralized by carbonate minerals in D₃x₄ waters. The TDS concentrations in the high-Sb D₃x₄ water ranged from 121 to 1515 mg/L, with an average of 542 mg/L, surpassing those found in the low-Sb D₃x₄ water samples (ranging from 254 to 331 mg/L, with an average of 300 mg/L).

The concentration of Sb showed no significant differences among HDOM, MDOM, and LDOM in the low-Sb D₃x₄ water (Fig. 2a). There was a slight decrease during sequential ultrafiltration in the high-Sb D₃x₄ water, and a slight decrease was observed during sequential ultrafiltration in the high-Sb D₃x₄ water, suggesting that Sb predominantly existed as a truly dissolved form in the LDOM D₃x₄ water. These findings align with the research conducted by Zhang et al. [63] and Jia et al. [50] on Sb migration as well as the study by Li et al. [33] on As presence in shallow groundwater.

A decrease in DOM concentration was noted in LDOM and MDOM D₃x₄ waters compared to HDOM D₃x₄ water (Fig. 2c), suggesting that the HDOM D₃x₄ water exhibited the highest level of DOM content. The majority of TFe detected in the extracts was observed in the HDOM D₃x₄ water (Fig. 2b), which experienced a significant decrease in both MDOM and LDOM D₃x₄ waters. This suggested that TFe predominantly existed as large colloids within the HDOM D₃x₄ water [33, 35, 50, 63, 64]. The consistent trends between DOM and TFe indicate that TFe may have a higher affinity for binding with HDOM in the D₃x₄ water [35]. Earlier research had established that substances found in HDOM, such as humic-like and fulvic acids, exhibited a preference for forming DOM-Fe complexes with Fe hydroxides in groundwater [17, 35, 65, 66]. Therefore, it can be deduced that TFe predominantly exists as colloidal particles attached to HDOM in the D₃x₄ water [40]. However, the distribution of Sb in the D₃x₄ water with varying pore sizes exhibited distinct variations compared to the distributions of TFe and DOC as depicted in Fig. 2(a-c), indicating that HDOM was not a crucial factor for promoting Sb enrichment in the D₃x₄ water.

Fluorescence Characteristics of DOM with Different Molecular Weights

Fig. 3 showed the six main EEM peaks: Ex 266 (336)/Em 435 (Peak A, representing the C1 component)

Table 2. Descriptive statistics of the DOM components, SR, SUVA₂₅₄, BIX, HIX, and FI in D3x4 water in the Xikuangshan mine area.

Type	C1	C2	C3	C4	C5	C6	Protein:humic	Microbial:terrestrial	SUVA ₂₅₄	BIX	FI	HIX
	%											
HDOM samples (n = 20)												
Max	30.74	45.46	27.35	42.57	21.65	35.90	7.35	17.97	2.74	1.12	2.37	0.76
Min	3.72	12.89	2.23	0.92	1.04	0.51	0.29	0.73	0.56	0.76	1.50	0.12
Mean	22.34	22.86	17.36	20.46	10.84	6.14	1.07	2.39	1.33	0.91	1.78	0.57
SD	7.35	8.21	5.48	13.42	5.53	7.14	1.51	3.72	0.63	0.11	0.24	0.19
MDOM samples (n = 20)												
Max	34.87	46.55	27.11	52.28	27.81	6.74	4.17	8.08	3.28	1.35	3.17	0.88
Min	6.76	10.32	8.33	0.36	1.37	1.41	0.12	0.50	0.41	0.73	1.25	0.19
Mean	22.19	25.20	17.28	20.63	10.44	4.27	1.33	2.66	1.38	0.92	1.76	0.52
SD	10.04	9.77	6.16	16.39	6.80	1.76	1.27	2.32	0.73	0.16	0.37	0.21
LDOM samples (n = 20)												
Max	30.40	47.19	22.10	68.82	15.07	7.41	9.93	24.01	2.18	1.49	2.41	0.43
Min	2.30	15.65	3.88	5.15	3.87	1.53	0.16	0.36	0.93	0.19	0.78	0.36
Mean	16.87	29.55	13.72	28.28	7.71	3.87	2.25	4.59	0.65	1.00	1.63	0.63
SD	8.74	9.31	17.27	5.18	4.41	2.24	2.34	5.37	0.44	0.16	0.43	0.43

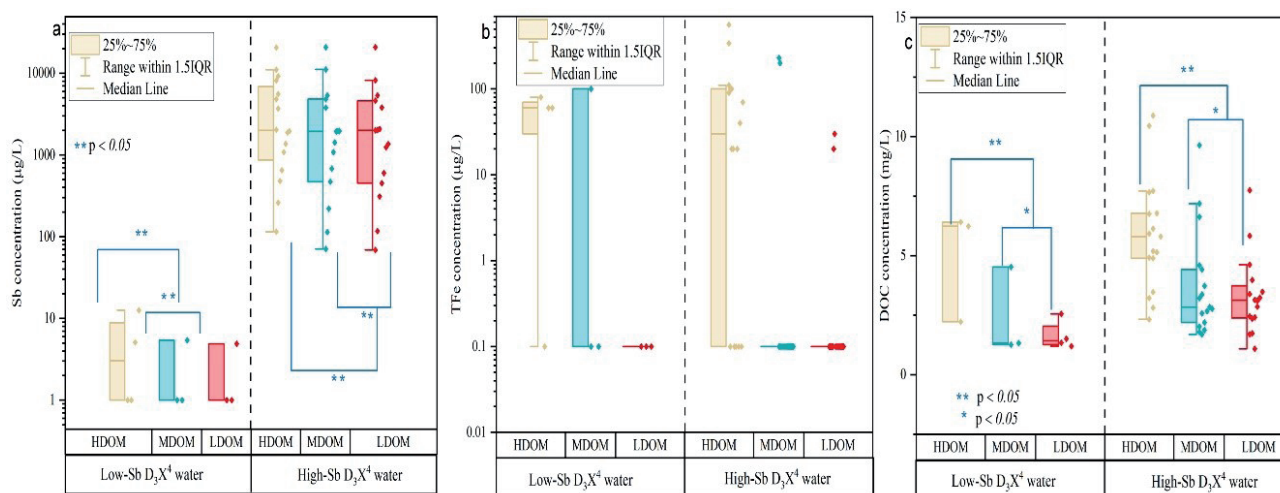


Fig. 2. Box-whisker plots of Sb a), TFe b), and DOC c) for different size fractions of DOM in D_3x^4 water.

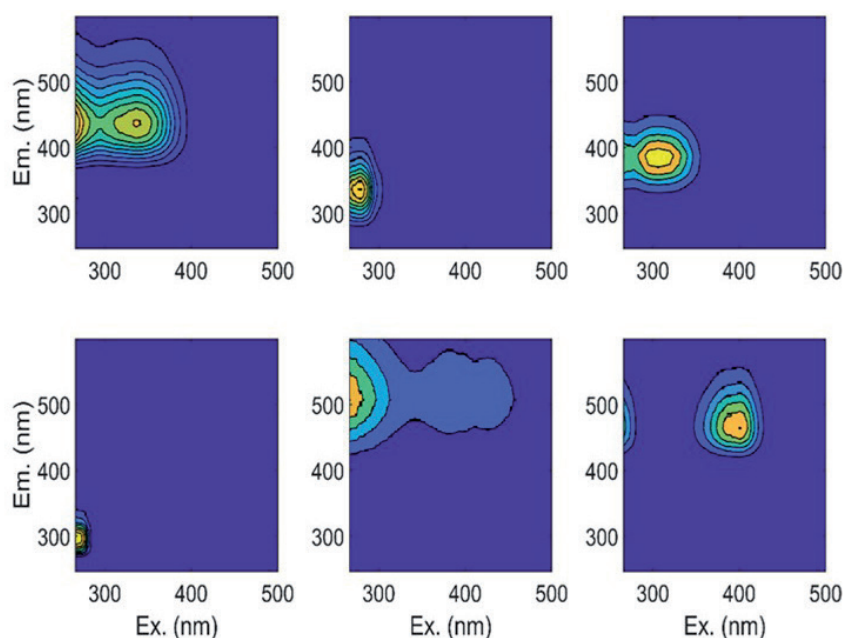


Fig. 3. Spectral properties of the six fluorophores identified by the PARAFAC analysis.

for the terrestrial humic-like component [37, 67, 68], Ex 278/Em 336 (Peak T, reflecting the C2 component) for the tryptophan-like substance [39, 69], Ex 306/Em 385 (Peak M, C3 component) for the microbial humic-like component [70, 71], Ex 266/Em 296 (Peak B, C4 component) for the carboxylic and phenolic groups component [32, 72], Ex 266/Em 507 (Peak C, C5 component) for the marine humic acid-like component [73, 74], and Ex 400/Em 464 (Peak D, C6 component) for the fulvic acid component [34, 64].

SUVA₂₅₄, BIX, FI, and HIX of DOM with different molecular weights were shown in Fig. 4. During the process of sequential ultrafiltration, there was a slight increase observed in BIX, SUVA₂₅₄, and HIX for low-Sb D_3x^4 waters (Fig. 4a–d), while a significant decrease was observed for high-Sb D_3x^4 waters. Significantly,

the HDOM exhibited mean values of SUVA₂₅₄ and HIX that were 2.65 and 1.27 times higher in the HDOM D_3x^4 water than those observed in the LDOM D_3x^4 water, respectively, suggesting a more pronounced presence of macromolecular aromatic substances in the HDOM D_3x^4 water. The rate of increase in BIX was found to be higher in the low-Sb D_3x^4 water compared to the high-Sb D_3x^4 water during the sequential ultrafiltration process (Fig. 4b), indicating the presence of biological and aquatic bacterial sources of DOM played a significant role in enriching Sb levels in the low-Sb D_3x^4 water [17, 27]. The FI values of both low- and high-Sb D_3x^4 water samples exhibited a wide range from 1.40 to 1.90, indicating the presence of terrestrial and microbial contributions (Fig. 4c). This suggests that the main sources of DOM in the D_3x^4 water are likely dominantly

derived from terrestrial and microorganism origins [37, 43]. During the sequential ultrafiltration process, there was a slight transition in the FI values from terrestrially and microbially derived zones to microbially derived zones in high-Sb D_3x^4 water (Fig. 4c), suggesting a greater contribution from microbial sources in LDOM D_3x^4 water.

As indicated in Table 2 and Fig. 5a), the PARAFAC components of DOM were dominated by humic-like and fulvic acid components (the combined percentages of C1, C3, C5, and C6), followed by protein-like components (the sum percentages of C2 and C4) in HDOM and MDOM D_3x^4 waters, whereas the contents of protein-like components considerably increased and became predominant in the LDOM D_3x^4 water. The observation provided additional evidence that the protein-like constituents exhibited a progressive increase in dominance and promotion in the LDOM D_3x^4 water, whereas humic-like and fulvic acid components were predominantly present in HDOM D_3x^4 water throughout the sequential ultrafiltration process [17, 75]. Previous studies have established that the majority of humic-like and fulvic acid components are present in the colloidal fraction, which can be effectively captured through ultrafiltration utilizing membranes with a molecular weight cut-off of 1 kDa [35].

In Fig. 5b), the percentages of C2 and C4 significantly increased with the decrease in ultrafilter pore size, while the abundances of C1, C3, C5, and C6

declined during the sequential ultrafiltration process. For the given samples, there was a significant increase in the proportion of C4, accompanied by notable decreases in abundances of C1 and C3, when compared to the relative proportions of other components in the LDOM D_3x^4 water. This indicated that the LDOM D_3x^4 water contained a higher proportion of the tyrosine-like component, while the HDOM and MDOM D_3x^4 water favored the presence of humic-like components as large colloids [3, 40, 64]. The observed variations in the relative of the humic-like and fulvic acids, as well as protein-like components, were attributed to changes occurring during the sequential ultrafiltration process in Fig. 5a) and Table 2. As depicted in Figure 5c, the proportions of protein:humic and microbial:terrestrial progressively rose with the reduction in ultrafilter pore size, providing confirmation that the LDOM D_3x^4 water primarily contained a protein-like component derived from microorganisms.

In general, the HDOM D_3x^4 water exhibited higher levels of HIX, $SUVA_{254}$, and percentages of C1 and C3, while lower levels of BIX, FI, and percentages of C2 and C4 were observed compared to the LDOM D_3x^4 water. This suggests that HDOM exhibited elevated levels of humification and aromaticity levels whereas LDOM was influenced by the microbial origin of DOM [33]. A similar outcome was observed in the Hetao Basin [33, 76], demonstrating that the chemical

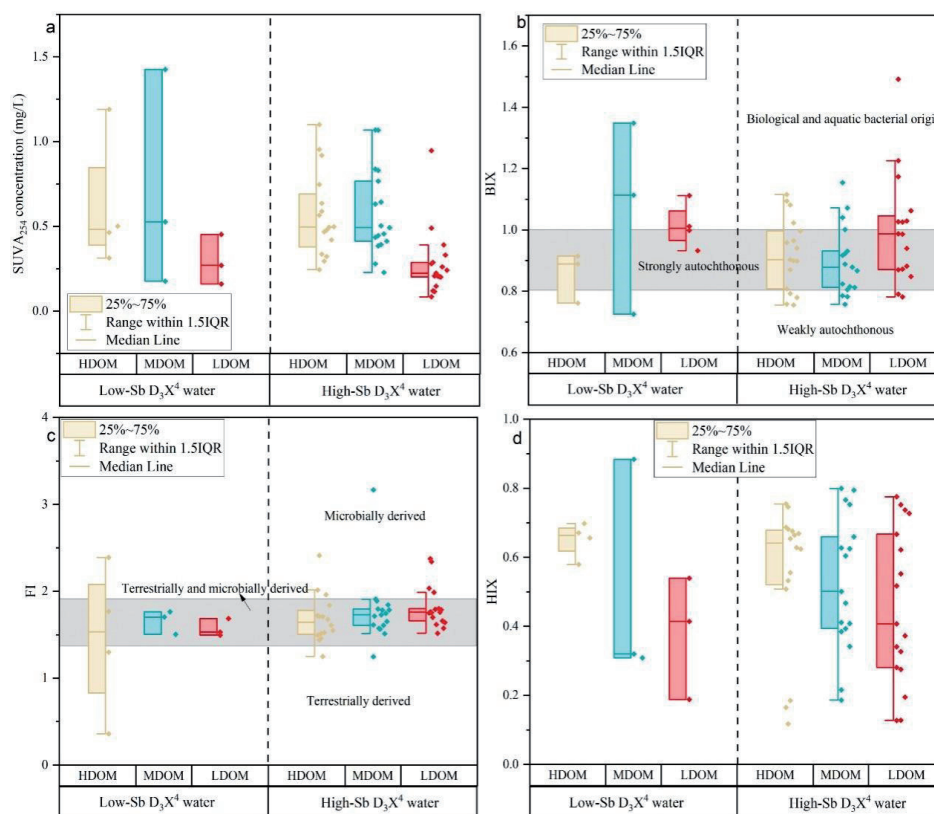


Fig. 4. Box-whisker plots of $SUVA_{254}$ a), BIX b), FI c), and HIX d) for different size fractions of DOM in D_3x^4 water.

characteristics of DOM with distinct molecular weights may have similar effects on the fates of As and Sb.

Discussion

DOMs with Different Molecular Weights as a Complexing Agent for Sb

As depicted in Fig. 2a) and b), the majority of TFe was observed as Fe hydroxides in the HDOM D_3x^4 water, while Sb was predominantly present in the LDOM D_3x^4 water. Meanwhile, there were slight correlations between Sb, DOC, and TFe in the HDOM D_3x^4 water (Fig. 6a) and a significant positive correlation ($R^2 = 0.48$) was found between Sb and DOC in the LDOM D_3x^4 water (Fig.6b), suggesting that the presence of enriched

TFe hydroxides had minimal impact on the migration of Sb within the LDOM and MDOM D_3x^4 water. This contrasted with the findings of Li et al. [33] in their study on a high As groundwater from the Hetao basin, where they observed that higher binding capacity for As was demonstrated by larger Fe colloids (>10 kDa) during the sequential ultrafiltration process. The phenomenon implied that As exhibited a tendency to form stronger associations with Fe complexes compared to Sb, owing to DOM with different molecular properties.

Compared to low-Sb D_3x^4 water samples, TFe mean concentrations in high-Sb D_3x^4 water samples were found 3.14 times higher, indicating that Sb was likely associated with TFe hydroxides and complexes formed by DOM in high-Sb D_3x^4 water samples. Humic-like components could form DOM-Fe-Sb complexes by complexing with Fe hydroxides and Sb [17, 23, 63, 77].

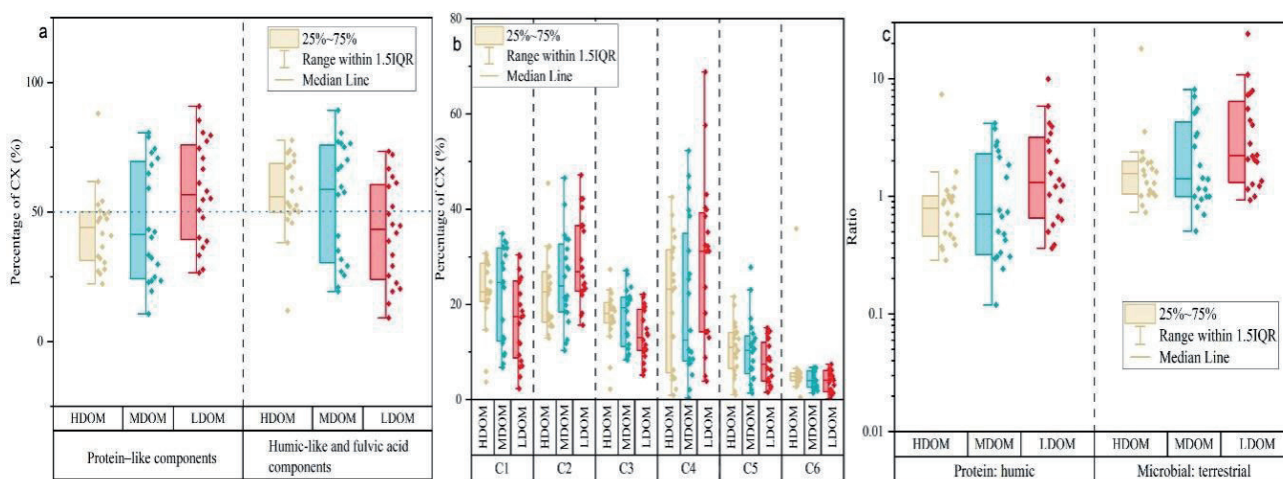


Fig. 5. Box-whisker plots of CX percentages for different size fractions of DOM in D_3x^4 water.

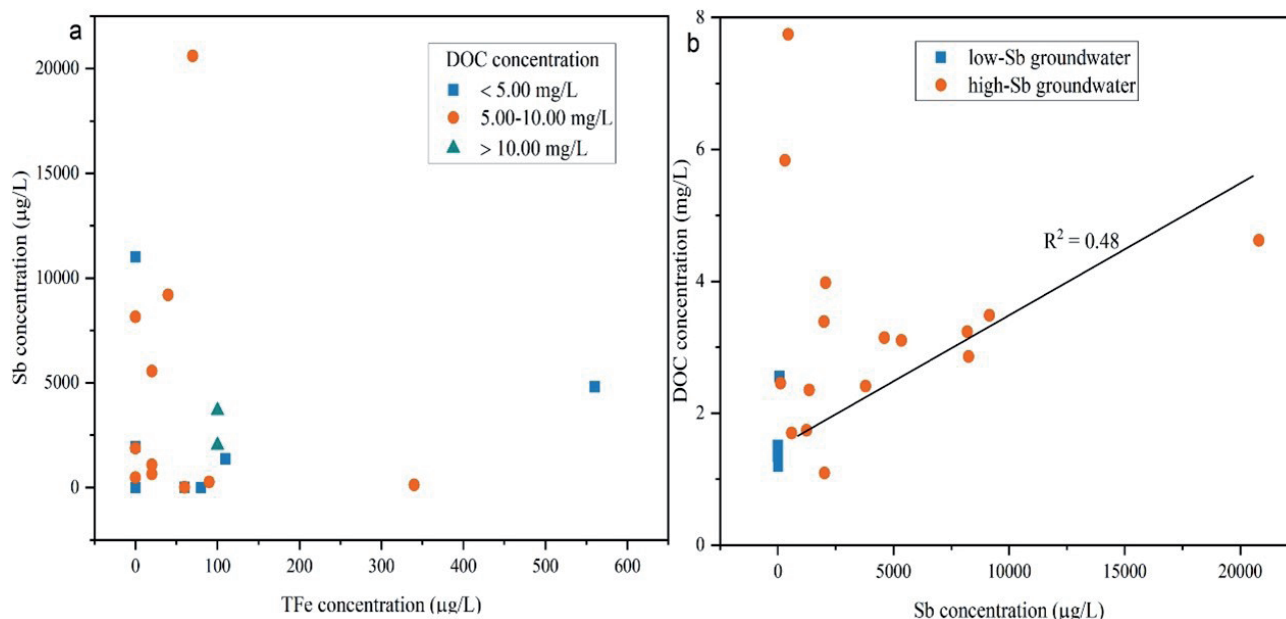


Fig. 6. a) Sb versus TFe concentration in the HDOM D_3x^4 water and b) Sb versus DOC concentration in the LDOM D_3x^4 water.

This finding aligns with the observed higher values of HIX and $SUVA_{254}$, as well as lower values of BIX and protein:humic ratio in the HDOM D_3x^4 water sample (Fig. 4a, b, d, and Fig. 5a). Complexes between Sb and humic-like substances of DOM are typically formed via the presence of positively charged amino groups in the DOM or metal cation bridges [20, 26, 40]. The interaction strength and durability of the binding between DOM and Sb were notably increased in groundwater through ligand substitution, the creation of negatively charged complexes, and the presence of bound hydrogen bridges [63, 78, 79].

In addition, the Sb concentration in the LDOM D_3x^4 water showed weak ($R^2 = 0.14$) and moderate ($R^2 = 0.32$) positive correlations with the percentages of C2 and C4, respectively in Fig. 7a and b. This suggested that protein-like component substances of DOM with lower HIX and $SUVA_{254}$ and higher percentages of C2 and C4 may contribute to an increase in Sb levels in the LDOM D_3x^4 water. These protein-like substances are known for their strong affinity, such as copper and cadmium [20, 36, 80, 81]. Furthermore, the stable Sb(III) could be rapidly oxidized to an easily mobile Sb(V) in the presence of the quinone groups in neutral and alkaline waters, resulting in Sb concentration enrichment in the LDOM D_3x^4 water [23, 78, 82].

The changes in fluorescent intensity for the six PARAFAC-derived components during the increase in Sb concentration were illustrated in Fig. 7c), specifically focusing on the LDOM D_3x^4 water. The quenching curves exhibited a significant correlation with the origins of DOM sources. The initial decrease in fluorescent intensities of C4 and C2 was followed by a gradual decrease and stabilization as the concentration of Sb increased. Conversely, there was a slight increase in the fluorescent intensities of C3 and an increase in Sb concentration, which could be attributed to the combination of Sb with DOM [19, 83]. Weak quenching effects were observed for C1 and C6. These results

suggested that the protein-like substances had more significant quenching effects than the humic-like materials in the LDOM D_3x^4 water.

In addition, the quenching levels of C4 were pronounced compared to those of C2, suggesting that the carboxylic and phenolic groups exhibited a stronger affinity for Sb in the LDOM D_3x^4 water [58, 81, 83]. Generally, the abundant presence of carboxylic and phenolic groups in DOM led to its high binding affinity towards heavy metals [58, 84], indicating the C4 component in the LDOM D_3x^4 water may be attributed to higher carboxylic and phenolic groups than other components. Moreover, the presence of carboxylic and phenolic groups on the C4 component may potentially hinder the adsorption onto TFe hydroxide surfaces, leading to the liberation of previously adsorbed Sb into the D_3x^4 water [17, 85].

Bioreactivity of LDOM and Microorganism Roles

Previous studies had proved the substances resembling proteins, characterized by a high BIX and low HIX and $SUVA_{254}$ values, along with significant bioreactivity, were found to enhance the Sb mobility in groundwater systems by facilitating electron transfer and energy acquisition for microbial degradation and activities [30]. Generally, microbial degradation of organic matter causes a lower $\delta^{13}C_{DIC}$ and higher $\delta^{13}C_{DOC}$ in groundwater, reflecting an active microbial process [54, 86, 87].

As depicted in Fig. 8a), the <1 kDa fractions exhibited elevated $\delta^{13}C_{DOC}$ values and almost unchanged $\delta^{13}C_{DIC}$ values during the sequential ultrafiltration process, suggesting a more pronounced microbial influence on DOM within the LDOM D_3x^4 water. The observed fluctuations in $\delta^{13}C_{DOC}$ may be ascribed to the surface-driven microbial oxidation of organic substances occurring within the shallow groundwater. Extensive regions of rice, corn, and vegetables were

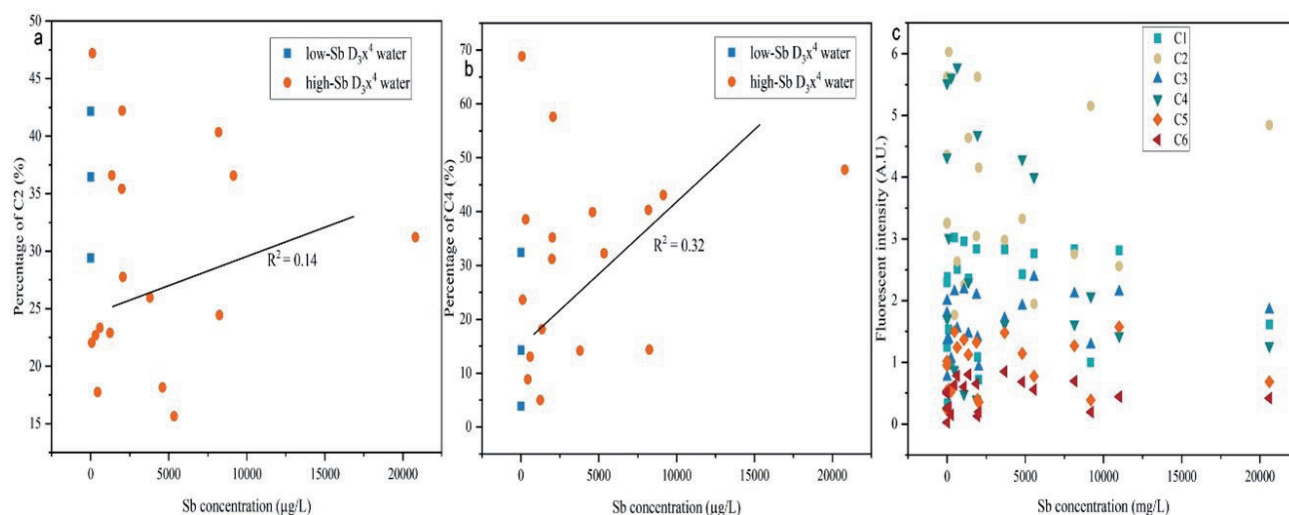


Fig. 7. a) Percentage of C2, b) percentage of C2, and c) fluorescence intensity versus Sb concentration in the LDOM D_3x^4 water.

allocated within the upper weathering zone of the D_3x^4 water. The input of DOM from precipitation may stimulate microbial respiration, resulting in an increase in $\delta^{13}C_{DOC}$ levels [88]. On the other hand, Sb with different valence states served as substrates for electron transfer and energy acquisition by autotrophic species in the oligotrophic groundwater environment [2, 30, 89]. The TFe levels in the LDOM D_3x^4 water varied from undetectable to 30.00 $\mu\text{g/L}$ (with an average of 2.59 $\mu\text{g/L}$), creating favorable conditions for microbial degradation through its interaction with Fe oxides and DOM [33, 89]. Furthermore, oxidative stibnite, serving as the primary mineral containing antimony, could have potentially acted as a significant energy provider for autotrophic communities through the discharge of antimony and sulfur compounds into the D_3x^4 water environment [2, 30].

In Fig. 8b), a noticeable decline in the difference between $\delta^{13}C_{DIC}$ and $\delta^{13}C_{DOC}$ was observed in the LDOM

D_3x^4 water as the Sb content increased ($R^2 = 0.72$), suggesting Sb mobilization was related to the degree of microbial degradation of DOM [54, 90]. The lower difference between $\delta^{13}C_{DIC}$ and $\delta^{13}C_{DOC}$ suggests a higher level of microbial degradation of DOM, even though the isotopic variation in organic carbon is minimal and can be disregarded during microbial degradation processes [54, 91, 92]. The correlation between $\delta^{13}C_{DIC}$ and the difference between $\delta^{13}C_{DIC}$ and $\delta^{13}C_{DOC}$ was found to be significantly positive, indicating that the oxidative decomposition of organic carbon played an important role in the reduction in $\delta^{13}C_{DIC}$. In the process of microbial degradation of DOM, microorganisms exhibited a preference for lighter carbon isotopes (^{12}C), leading to decreased $\delta^{13}C_{DIC}$ levels and increased concentrations of HCO_3^- in groundwater [80, 93]. Compared to the low-Sb D_3x^4 water, the high-Sb D_3x^4 water exhibited lower and more negative $\delta^{13}C_{DIC}$ subtracted by $\delta^{13}C_{DOC}$, indicating that the microbial degradation of DOM played a crucial

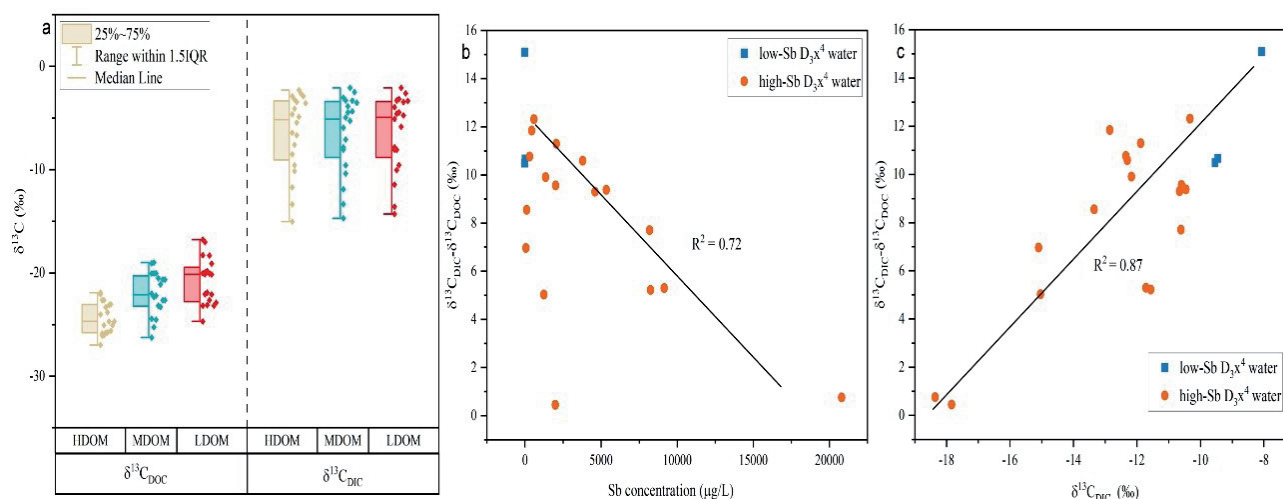


Fig. 8. a) Box-whisker plots of CX percentages for different size fractions of DOM, b) relationship between $\delta^{13}C_{DIC} - \delta^{13}C_{DOC}$ and Sb concentration, and c) relationship between $\delta^{13}C_{DIC} - \delta^{13}C_{DOC}$ and $\delta^{13}C_{DIC}$ in the LDOM D_3x^4 water.

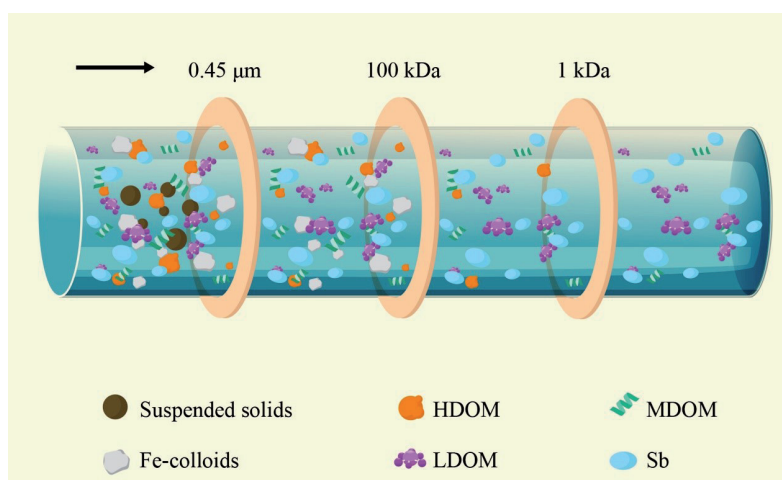


Fig. 9. The sequential ultrafiltration process of DOM with different molecular weights for Sb migration in D_3x^4 water.

role in the mobilization and enrichment of Sb in the LDOM D_3x^4 water [2, 17, 30].

Therefore, our results suggested that Sb was primarily bound to protein-like substances with biological activity and is influenced by microbial degradation in the LDOM D_3x^4 water. As a result, the changes in Sb concentration were not found to be significant throughout the sequential ultrafiltration process (Fig.9). However, the impact of TFe was not ignored, which could play a role in facilitating the combination of Sb and DOM. This combination forms a Fe bridge, thereby promoting the accumulation of Sb in HDOM and MDOM D_3x^4 waters.

Conclusions

In this investigation, the majority of Sb was detected in the LDOM D_3x^4 water, while TFe colloids and DOC were mostly present in the HDOM and MDOM D_3x^4 water, respectively. The findings suggested that the presence of large Fe colloids or HDOM did not play a significant role in the enrichment of Sb in the D_3x^4 water. The LDOM D_3x^4 water, exhibiting elevated BIX and higher proportions of C2 and C4, and reduced HIX, percentages of C1 and C3 with a pronounced presence of protein-like substances, demonstrated compatibility for the formation of complexes with Sb. The quenching levels of C4 constituents generally surpassed those of C2, which showed that the carboxylic and phenolic groups exhibited an affinity for Sb in the LDOM D_3x^4 water.

During the sequential ultrafiltration process, higher $\delta^{13}C_{DOC}$ and lower $\delta^{13}C_{DIC}$ values were observed in the <1 kDa fractions. Additionally, in the high-Sb D_3x^4 water, there was a decrease in both $\delta^{13}C_{DIC}$ subtracted by $\delta^{13}C_{DOC}$ and $\delta^{13}C_{DIC}$ values. This suggests that microbial degradation of DOM played a significant role in influencing the mobility of Sb in the D_3x^4 water.

Despite molecular weight fractions of DOM may provide insights into its roles on Sb mobility, our findings are limited, and the molecular characteristics and mechanisms of DOM on Sb enrichment remain unclear. Overall, these discoveries will enhance comprehension of the biogeochemical actions of Sb and offer valuable perspectives for effectively managing shallow groundwater environments and ensuring the safety of drinking water within the study area.

Acknowledgments

This work was supported by the Natural Science Foundation of Hebei Province (D2021508004), Open Foundation of Key Laboratory of Mine Geological Hazards Mechanism and Control Project (2022-09), the Key Laboratory of Natural Resource Coupling Process and Effects (No.2023KFKTB005), and the ecological restoration project in the Lengshuijiang antimony mine area (Grant LCG2020009).

Conflict of Interest

The authors declare no conflict of interest.

References

- HAO C., GUI H., SHENG L., MIAO J., LIAN H. Contrasting water – rock interaction behaviors of antimony and arsenic in contaminated rivers around an antimony mine, Hunan Province, China. *Geochemistry*, **81** (2), **2021**.
- HE M., WANG N., LONG X., ZHANG C., MA C., ZHONG Q., WANG A., WANG Y., PERVAIZ A., SHAN J. Antimony speciation in the environment: Recent advances in understanding the biogeochemical processes and ecological effects. *Journal of Environmental Sciences*, **75**, 14, **2019**.
- WANG Y., ZHANG G., WANG H., CHENG Y., LIU H., JIANG Z., LI P., WANG Y. Effects of different dissolved organic matter on microbial communities and arsenic mobilization in aquifers. *Journal of Hazardous Materials*, **411**, **2021**.
- WEN B., ZHOU J., JIA X., ZHOU W., HUANG Y. Attenuation of antimony in groundwater from the Xikuangshan antimony mine, China: Evidence from sulfur and molybdenum isotope study. *Applied Geochemistry*, **146**, **2022**.
- WEN B., ZHOU J., ZHOU A., LIU C., XIE L. Sources, migration and transformation of antimony contamination in the water environment of Xikuangshan, China: Evidence from geochemical and stable isotope (S, Sr) signatures. *Science of The Total Environment*, **569-570**, 114, **2016**.
- HAO C., ZHANG W., GUI H. Hydrogeochemistry characteristic contrasts between low- and high-antimony in shallow drinkable groundwater at the largest antimony mine in hunan province, China. *Applied Geochemistry*, **117**, **2020**.
- JOHNSTON S.G., BENNETT W.W., DORIEAN N., HOCKMANN K., KARIMIAN N., BURTON E.D. Antimony and arsenic speciation, redox-cycling and contrasting mobility in a mining-impacted river system. *Science of The Total Environment*, **710**, **2020**.
- MACGREGOR K., MACKINNON G., FARMER J.G., GRAHAM M.C. Mobility of antimony, arsenic and lead at a former antimony mine, Glendinning, Scotland. *Science of The Total Environment*, **529**, 213, **2015**.
- MASSON M., SCHÄFER J., BLANC G., DABRIN A., CASTELLE S., LAVAUX G. Behavior of arsenic and antimony in the surface freshwater reaches of a highly turbid estuary, the Gironde Estuary, France. *Applied Geochemistry*, **24** (9), 1747, **2009**.
- PALMER M.J., CHÉTELAT J., RICHARDSON M., JAMIESON H.E., GALLOWAY J.M. Seasonal variation of arsenic and antimony in surface waters of small subarctic lakes impacted by legacy mining pollution near Yellowknife, NT, Canada. *Science of The Total Environment*, **684**, 326, **2019**.
- BORČINOVÁ RADKOVÁ A., JAMIESON H.E., CAMPBELL K.M. Antimony mobility during the early stages of stibnite weathering in tailings at the Beaver Brook Sb deposit, Newfoundland. *Applied Geochemistry*, **115**, **2020**.
- CIDU R., BIDDAU R., DORE E., VACCA A., MARINI L. Antimony in the soil-water-plant system at the Su Suergiu abandoned mine (Sardinia, Italy): Strategies to mitigate

- contamination. *Science of The Total Environment*, **497-498**, 319, **2014**.
13. EL-BADRY A.E.-M.A., KHALIFA M.M. The occurrence and distribution of high-arsenic, selenium, tin and antimony in bottom sediments of Burullus lagoon and its effects on human health, Egypt. *Journal of African Earth Sciences*, **136**, 305, **2017**.
 14. HU X., HE M., KONG L. Photopromoted oxidative dissolution of stibnite. *Applied Geochemistry*, **61**, 53, **2015**.
 15. HU X., HE M., LI S., GUO X. The leaching characteristics and changes in the leached layer of antimony-bearing ores from China. *Journal of Geochemical Exploration*, **176**, 76, **2017**.
 16. NISHAD P.A., BHASKARAPILLAI A. Antimony, a pollutant of emerging concern: A review on industrial sources and remediation technologies. *Chemosphere*, **277**, **2021**.
 17. HAO C., LIU M., PENG Y., WEI Z. Comparison of Antimony Sources and Hydrogeochemical Processes in Shallow and Deep Groundwater Near the Xikuangshan Mine, Hunan Province, China. *Mine Water and the Environment*, **41** (1), 194, **2021**.
 18. HE M., WANG X., WU F., FU Z. Antimony pollution in China. *Science of The Total Environment*, **421-422**, 41, **2012**.
 19. HU B., WANG P.-F., ZHANG N.-N., BAO T.-L., JIN Q.-T. Binding Affinity Between Heavy Metal Hg and Dissolved Organic Matter in Hongze Lake. *Environmental Science*, **43** (5), 2510, **2022**.
 20. BUSCHMANN J., SIGG L. Antimony (III) binding to humic substances: Influence of pH and type of humic acid. *Environmental Science & Technology*, **38** (17), 4535, **2004**.
 21. FAN Y., ZHENG C., HUO A., WANG Q., SHEN Z., XUE Z., HE C. Investigating the binding properties between antimony(V) and dissolved organic matter (DOM) under different pH conditions during the soil sorption process using fluorescence and FTIR spectroscopy. *Ecotoxicology and Environmental Safety*, **181**, 34, **2019**.
 22. KARIMIAN N., BURTON E.D., JOHNSTON S.G., HOCKMANN K., CHOPPALA G. Humic acid impacts antimony partitioning and speciation during iron(II)-induced ferrihydrite transformation. *Science of The Total Environment*, **683**, 399, **2019**.
 23. WANG Y., KONG L., HE M., OUYANG W., LIN C., LIU X. Influences of Particles and Aquatic Colloids on the Oxidation of Sb(III) in Natural Water. *ACS Earth and Space Chemistry*, **4** (4), 661, **2020**.
 24. YANG H., LU X., HE M. Effect of organic matter on mobilization of antimony from nanocrystalline titanium dioxide. *Environmental Technology*, **39** (12), 1515, **2017**.
 25. CHU Y., ZHANG X., YU X., YAN C., YANG Y., SHEN G., WANG X., TAO S., WANG X. Antimony removal by a magnetic $\text{TiO}_2/\text{SiO}_2/\text{Fe}_3\text{O}_4$ nanosphere and influence of model dissolved organic matter. *Chemical Engineering Journal*, **420**, **2021**.
 26. KARIMIAN N., BURTON E.D., JOHNSTON S.G. Antimony speciation and mobility during Fe(II)-induced transformation of humic acid-antimony(V)-iron(III) coprecipitates. *Environmental Pollution*, **254**, **2019**.
 27. LIU H., ZENG W., HE M., LIN C., OUYANG W., LIU X. Occurrence, distribution, and migration of antimony in the Zijiang River around a superlarge antimony deposit zone. *Environmental Pollution*, **316**, **2023**.
 28. KONG L., HE M. Mechanisms of Sb(III) Photooxidation by the Excitation of Organic Fe(III) Complexes. *Environmental Science & Technology*, **50** (13), 6974, **2016**.
 29. LONI P.C., WU M., WANG W., WANG H., MA L., LIU C., SONG Y., TUOVINEN O.H., Mechanism of microbial dissolution and oxidation of antimony in stibnite under ambient conditions. *Journal of Hazardous Materials*, **385**, **2020**.
 30. WANG W., CHENG X., SONG Y., WANG H., WU M., MA L., LU X., LIU X., TUOVINEN O.H. Elevated antimony concentration stimulates rare taxa of potential autotrophic bacteria in the Xikuangshan groundwater. *Science of The Total Environment*, **864**, **2023**.
 31. GAO Z., GUÉGUEN C. Size distribution of absorbing and fluorescing DOM in Beaufort Sea, Canada Basin. *Deep Sea Research Part I: Oceanographic Research Papers*, **121**, 30, **2017**.
 32. CHEN T.-C., HSEU Z.-Y., JEAN J.-S., CHOU M.-L. Association between arsenic and different-sized dissolved organic matter in the groundwater of black-foot disease area, Taiwan. *Chemosphere*, **159**, 214, **2016**.
 33. LI X., GUO H., ZHENG H., XIU W., HE W., DING Q. Roles of different molecular weights of dissolved organic matter in arsenic enrichment in groundwater: Evidences from ultrafiltration and EEM-PARAFAC. *Applied Geochemistry*, **104**, 124, **2019**.
 34. TAREQ S.M., MARUO M., OHTA K. Characteristics and role of groundwater dissolved organic matter on arsenic mobilization and poisoning in Bangladesh. *Physics and Chemistry of the Earth, Parts A/B/C*, **58-60**, 77, **2013**.
 35. GONTIJO E.S.J., WATANABE C.H., MONTEIRO A.S.C., DA SILVA G.A., ROESER H.M.P., ROSA A.H., FRIESE K. Effects of Fe(III) and quality of humic substances on As(V) distribution in freshwater: Use of ultrafiltration and Kohonen neural network. *Chemosphere*, **188**, 208, **2017**.
 36. GUO H., LI X., XIU W., HE W., CAO Y., ZHANG D., WANG A. Controls of organic matter bioreactivity on arsenic mobility in shallow aquifers of the Hetao Basin, P.R. China. *Journal of Hydrology*, **571**, 448, **2019**.
 37. GAO Z., GUO H., QIAO W., HE C., SHI Q., KE T., CAO Y. Dissolved Organic Matter Sources in High Arsenic Groundwater From a Sand-Gravel Confined Aquifer. *Journal of Geophysical Research: Biogeosciences*, **128** (2), **2023**.
 38. FU Z., WU F., MO C., DENG Q., MENG W., GIESBY J.P. Comparison of arsenic and antimony biogeochemical behavior in water, soil and tailings from Xikuangshan, China. *Science of The Total Environment*, **539**, 97, **2016**.
 39. DU Y., ZHANG Q., LIU Z., HE H., LÜRLING M., CHEN M., ZHANG Y. Composition of dissolved organic matter controls interactions with La and Al ions: Implications for phosphorus immobilization in eutrophic lakes. *Environmental Pollution*, **248**, 36, **2019**.
 40. LI Y., GONG X., SUN Y., SHU Y., NIU D., YE H. High molecular weight fractions of dissolved organic matter (DOM) determined the adsorption and electron transfer capacity of DOM on iron minerals. *Chemical Geology*, **604**, **2022**.
 41. MAKEHELWALA M., WEI Y., WERAGODA S.K., WEERASOORIYA R., ZHENG L. Characterization of dissolved organic carbon in shallow groundwater of chronic kidney disease affected regions in Sri Lanka. *Science of The Total Environment*, **660**, 865, **2019**.
 42. JIANG T., SKYLLBERG U., BJÖRN E., GREEN N.W., TANG J., WANG D., GAO J., LI C. Characteristics of dissolved organic matter (DOM) and relationship with dissolved mercury in Xiaoqing River-Laizhou Bay estuary, Bohai Sea, China. *Environmental Pollution*, **223**, 19, **2017**.

43. MALIK A., PARVAIZ A., MUSHTAQ N., HUSSAIN I., JAVED T., REHMAN H. U., FAROOQI A. Characterization and role of derived dissolved organic matter on arsenic mobilization in alluvial aquifers of Punjab, Pakistan. *Chemosphere*, **251**, 2020.
44. RICHARDS L.A., LAPWORTH D.J., MAGNONE D., GODDY D.C., CHAMBERS L., WILLIAMS P.J., VAN DONGEN B.E., POLYA D.A. Dissolved organic matter tracers reveal contrasting characteristics across high arsenic aquifers in Cambodia: A fluorescence spectroscopy study. *Geoscience Frontiers*, **10** (5), 1653, 2019.
45. WALKER S.A., AMON R.M.W., STEDMON C., DUAN S., LOUCHOUARN P. The use of PARAFAC modeling to trace terrestrial dissolved organic matter and fingerprint water masses in coastal Canadian Arctic surface waters. *Journal of Geophysical Research: Biogeosciences*, **114** (G4), 2009.
46. LIU W., XIE X., WANG Y. Novel insight into arsenic enrichment in aquifer sediments under different paleotemperatures from a molecular-level characterization of sedimentary organic matter. *Journal of Hazardous Materials*, **451**, 2023.
47. FU Z., WU F., AMARASIRIWARDENA D., MO C., LIU B., ZHU J., DENG Q., LIAO H. Antimony, arsenic and mercury in the aquatic environment and fish in a large antimony mining area in Hunan, China. *Science of The Total Environment*, **408** (16), 3403, 2010.
48. GUO W., FU Z., WANG H., SONG F., WU F., GIESY J.P. Environmental geochemical and spatial/temporal behavior of total and speciation of antimony in typical contaminated aquatic environment from Xikuangshan, China. *Microchemical Journal*, **137**, 181, 2018.
49. WEN B., ZHOU J., ZHOU A., LIU C., LI L. A review of antimony (Sb) isotopes analytical methods and application in environmental systems. *International Biodeterioration & Biodegradation*, **128**, 109, 2018.
50. JIA X., MAJZLAN J., MA L., LIU P., FAN P., LI W., ZHOU J., WEN B. Novel insights into the mechanisms for Sb mobilization in groundwater in a mining area: A colloid field study. *Journal of Hazardous Materials*, **459**, 2023.
51. DÜNDAR O.A., MEHENKTAŞ C., ARAR Ö. Removal of Antimony(III) and Antimony(V) from water samples through water-soluble polymer-enhanced ultrafiltration. *Environmental Research*, **215**, 2022.
52. FAN J.-X., WANG Y.-J., FAN T.-T., DANG F., ZHOU D.-M. Effect of aqueous Fe(II) on Sb(V) sorption on soil and goethite. *Chemosphere*, **147**, 44, 2016.
53. YU K., DUAN Y., GAN Y., ZHANG Y., ZHAO K. Anthropogenic influences on dissolved organic matter transport in high arsenic groundwater: Insights from stable carbon isotope analysis and electrospray ionization Fourier transform ion cyclotron resonance mass spectrometry. *Science of The Total Environment*, **708**, 2020.
54. ZHOU Y., GUO H., ZHANG Z., LU H., JIA Y., CAO Y. Characteristics and implication of stable carbon isotope in high arsenic groundwater systems in the northwest Hetao Basin, Inner Mongolia, China. *Journal of Asian Earth Sciences*, **163**, 70, 2018.
55. SINGH S., INAMDAR S., SCOTT D. Comparison of Two PARAFAC Models of Dissolved Organic Matter Fluorescence for a Mid-Atlantic Forested Watershed in the USA. *Journal of Ecosystems*, **2013**, 1, 2013.
56. XU X., KANG J., SHEN J., ZHAO S., WANG B., ZHANG X., CHEN Z. EEM-PARAFAC characterization of dissolved organic matter and its relationship with disinfection by-products formation potential in drinking water sources of northeastern China. *Science of The Total Environment*, **774**, 2021.
57. PI K., WANG Y., XIE X., HUANG S., YU Q., YU M. Geochemical effects of dissolved organic matter biodegradation on arsenic transport in groundwater systems. *Journal of Geochemical Exploration*, **149**, 8, 2015.
58. HUANG M., LI Z., HUANG B., LUO N., ZHANG Q., ZHAI X., ZENG G. Investigating binding characteristics of cadmium and copper to DOM derived from compost and rice straw using EEM-PARAFAC combined with two-dimensional FTIR correlation analyses. *Journal of Hazardous Materials*, **344**, 539, 2018.
59. JIANG T., BRAVO A.G., SKYLLBERG U., BJÖRN E., WANG D., YAN H., GREEN N.W. Influence of dissolved organic matter (DOM) characteristics on dissolved mercury (Hg) species composition in sediment porewater of lakes from southwest China. *Water Research*, **146**, 146, 2018.
60. KELLERMAN A.M., KOTHAWALA D.N., DITTMAR T., TRANVIK L.J. Persistence of dissolved organic matter in lakes related to its molecular characteristics. *Nature Geoscience*, **8** (6), 454, 2015.
61. LI P., HUR J. Utilization of UV-Vis spectroscopy and related data analyses for dissolved organic matter (DOM) studies: A review. *Critical Reviews in Environmental Science and Technology*, **47** (3), 131, 2017.
62. LI S., MENG L., ZHAO C., GU Y., SPENCER R.G.M., ÁLVAREZ-SALGADO X.A., KELLERMAN A.M., MCKENNA A.M., HUANG T., YANG H., HUANG C. Spatiotemporal response of dissolved organic matter diversity to natural and anthropogenic forces along the whole mainstream of the Yangtze River. *Water Research*, **234**, 2023.
63. ZHANG C., WU P., YANG Z., LIU F., LUO H., LUO J. Effect of iron cyclic transformation on the natural purification of antimony in contaminated reservoirs of mines. *Science of The Total Environment*, **874**, 2023.
64. REN W., WU X., GE X., LIN G., ZHOU M., LONG Z., YU X., TIAN W. Characteristics of dissolved organic matter in lakes with different eutrophic levels in southeastern Hubei Province, China. *Journal of Oceanology and Limnology*, **39** (4), 1256, 2021.
65. LI Z., SHAKIBA S., DENG N., CHEN J., LOUIE S.M., HU Y. Natural Organic Matter (NOM) Imparts Molecular-Weight-Dependent Steric Stabilization or Electrostatic Destabilization to Ferrihydrite Nanoparticles. *Environmental Science & Technology*, **54** (11), 6761, 2020.
66. QIAO W., CAO W., GAO Z., PAN D., REN Y., LI Z., ZHANG Z. Contrasting behaviors of groundwater arsenic and fluoride in the lower reaches of the Yellow River basin, China: Geochemical and modeling evidences. *Science of The Total Environment*, **851**, 2022.
67. ZHUANG W.-E., CHEN W., CHENG Q., YANG L. Assessing the priming effect of dissolved organic matter from typical sources using fluorescence EEMs-PARAFAC. *Chemosphere*, **264**, 2021.
68. SMITH M.A., KOMINOSKI J.S., GAISER E.E., PRICE R.M., TROXLER T.G. Stormwater Runoff and Tidal Flooding Transform Dissolved Organic Matter Composition and Increase Bioavailability in Urban Coastal Ecosystems. *Journal of Geophysical Research: Biogeosciences*, **126** (7), 2021.
69. RYAN K.A., PALACIOS L.C., ENCINA F., GRAEBER D., OSORIO S., STUBBINS A., WOELFL S., NIMPTSCH J. Assessing inputs of aquaculture-derived nutrients to

- streams using dissolved organic matter fluorescence. *Science of The Total Environment*, **807**, 2022.
70. GROENEVELD M., CATALÁN N., ATTERMEYER K., HAWKES J., EINARSDÓTTIR K., KOTHAWALA D., BERGQUIST J., TRANVIK L. Selective Adsorption of Terrestrial Dissolved Organic Matter to Inorganic Surfaces Along a Boreal Inland Water Continuum. *Journal of Geophysical Research: Biogeosciences*, **125** (3), 2020.
 71. MEILLEUR C., KAMULA M., KUZYK Z.A., GUÉGUEN C. Insights into surface circulation and mixing in James Bay and Hudson Bay from dissolved organic matter optical properties. *Journal of Marine Systems*, **238**, 2023.
 72. HARSHA M.L., REDMAN Z.C., WESOŁOWSKI J., PODGORSKI D.C., TOMCO P.L. Photochemical formation of water-soluble oxyPAHs, naphthenic acids, and other hydrocarbon oxidation products from Cook Inlet, Alaska crude oil and diesel in simulated seawater spills. *Environmental Science: Advances*, **2** (3), 447, 2023.
 73. CAWLEY K.M., DING Y., FOURQUREAN J., JAFFÉ R. Characterising the sources and fate of dissolved organic matter in Shark Bay, Australia: a preliminary study using optical properties and stable carbon isotopes. *Marine and Freshwater Research*, **63** (11), 2012.
 74. OSBURN C.L., HANDSEL L.T., PEIERLS B.L., PAERL H.W. Predicting Sources of Dissolved Organic Nitrogen to an Estuary from an Agro-Urban Coastal Watershed. *Environmental Science & Technology*, **50** (16), 8473, 2016.
 75. LI X., PAN G., ZHOU A., FANG L., HE N. Stable sulfur and oxygen isotopes of sulfate as tracers of antimony and arsenic pollution sources related to antimony mine activities in an impacted river. *Applied Geochemistry*, **142**, 2022.
 76. QIAO W., GUO H., HE C., SHI Q., ZHAO B. Unraveling roles of dissolved organic matter in high arsenic groundwater based on molecular and optical signatures. *Journal of Hazardous Materials*, **406**, 2021.
 77. FAN J.-X., WANG Y.-J., FAN T.-T., CUI X.-D., ZHOU D.-M. Photo-induced oxidation of Sb(III) on goethite. *Chemosphere*, **95**, 295, 2014.
 78. BUSCHMANN J., CANONICA S., SIGG L. Photoinduced oxidation of antimony (III) in the presence of humic acid. *Environmental Science & Technology*, **39** (14), 5335, 2005.
 79. WU T.-L., SUN Q., FANG G.-D., CUI P.-X., LIU C., ALVES M.E., QIN W.-X., ZHOU D.-M., SHI Z.-Q., WANG Y.-J. Unraveling the effects of gallic acid on Sb(III) adsorption and oxidation on goethite. *Chemical Engineering Journal*, **369**, 414, 2019.
 80. ZAVADLAV S., KANDUČ T., MCINTOSH J., LOJEN S. Isotopic and Chemical Constraints on the Biogeochemistry of Dissolved Inorganic Carbon and Chemical Weathering in the Karst Watershed of Krka River (Slovenia). *Aquatic Geochemistry*, **19** (3), 209, 2013.
 81. WU J., ZHANG H., HE P.-J., SHAO L.-M. Insight into the heavy metal binding potential of dissolved organic matter in MSW leachate using EEM quenching combined with PARAFAC analysis. *Water Research*, **45** (4), 1711, 2011.
 82. WU T.-L., QIN W.-X., ALVES M.E., FANG G.-D., SUN Q., CUI P.-X., LIU C., ZHOU D.-M., WANG Y.-J. Mechanisms of Sb(III) oxidation mediated by low molecular weight phenolic acids. *Chemical Engineering Journal*, **356**, 190, 2019.
 83. BAO T., WANG P., HU B., SHI Y. Investigation on the effects of sediment resuspension on the binding of colloidal organic matter to copper using fluorescence techniques. *Chemosphere*, **236**, 2019.
 84. GUO X.-J., HE X.-S., LI C.-W., LI N.-X. The binding properties of copper and lead onto compost-derived DOM using Fourier-transform infrared, UV-vis and fluorescence spectra combined with two-dimensional correlation analysis. *Journal of Hazardous Materials*, **365**, 457, 2019.
 85. KARIMIAN N., JOHNSTON S.G., TAVAKKOLI E., FRIERDICH A.J., BURTON E.D. Mechanisms of arsenic and antimony co-sorption onto jarosite: An X-ray absorption spectroscopic study. *Environmental Science & Technology*, **57** (12), 4813, 2023.
 86. MAO R., GUO H., XIU W., YANG Y., HUANG X., ZHOU Y., LI X., JIN J. Characteristics and compound-specific carbon isotope compositions of sedimentary lipids in high arsenic aquifers in the Hetao basin, Inner Mongolia. *Environmental Pollution*, **241**, 85, 2018.
 87. PATHAK P., GHOSH P., SWARAJ A., YU T.-L., SHEN C.-C. Role of carbon and sulfur biogeochemical cycles on the seasonal arsenic mobilization process in the shallow groundwater of the Bengal aquifer. *Applied Geochemistry*, **141**, 2022.
 88. XIE X., WANG Y., ELLIS A., LI J., SU C., DUAN M. Multiple isotope (O, S and C) approach elucidates the enrichment of arsenic in the groundwater from the Datong Basin, northern China. *Journal of Hydrology*, **498**, 103, 2013.
 89. LI J., WANG Q., OREMLAND R.S., KULP T.R., RENSING C., WANG G., DRAKE H.L. Microbial Antimony Biogeochemistry: Enzymes, Regulation, and Related Metabolic Pathways. *Applied and Environmental Microbiology*, **82** (18), 5482, 2016.
 90. GUO H., ZHANG D., WEN D., WU Y., NI P., JIANG Y., GUO Q., LI F., ZHENG H., ZHOU Y. Arsenic mobilization in aquifers of the southwest Songnen basin, P.R. China: Evidences from chemical and isotopic characteristics. *Science of The Total Environment*, **490**, 590, 2014.
 91. HILL J.M., MCQUAID C.D. Variability in the fractionation of stable isotopes during degradation of two intertidal red algae. *Estuarine, Coastal and Shelf Science*, **82** (3), 397, 2009.
 92. BOTSCH K.C., CONRAD R. Fractionation of stable carbon isotopes during anaerobic production and degradation of propionate in defined microbial cultures. *Organic Geochemistry*, **42** (3), 289, 2011.
 93. LI S.-L., LIU C.-Q., LANG Y.-C., TAO F., ZHAO Z., ZHOU Z. Stable Carbon Isotope Biogeochemistry and Anthropogenic Impacts on Karst Ground Water, Zunyi, Southwest China. *Aquatic Geochemistry*, **14** (3), 211, 2008.